Computing extracellular electrical potentials from neuronal simulations

Geir Halnes[a,b], Torbjørn V. Ness[a], Solveig Næss[b], Klas H. Pettersen[c], Gaute T. Einevoll[a,b,d,*]

[a] *Faculty of Science and Technology, Norwegian University of Life Sciences, Ås, Norway*
[b] *Center for Integrative Neuroplasticity, University of Oslo, Oslo, Norway*
[c] *Norwegian Artificial Intelligence Research Consortium, Oslo, Norway*
[d] *Department of Physics, University of Oslo, Oslo, Norway*

Abstract

Measurements of electric potentials from neural activity have played a key role in neuroscience for almost a century, and simulations of neural activity is an important tool for understanding such measurements. Volume conductor (VC) theory is used ~~in neuroscience~~ to compute extracellular electrical potentials such as extracellular spikes, MUA, LFP, ECoG and EEG, and also during analysis of recorded potentials for reconstructing the neuronal current sources through current source density methods. In this book chapter, we show how VC theory can be derived from a detailed electrodiffusive theory for ion concentration dynamics in the extracellular medium, and show what assumptions that must be introduced to get the VC theory on the simplified form that is commonly used by neuroscientists. Furthermore, we provide examples of how the theory is applied, using the Python tool LFPy TVN: jeg pleier aa tenke at aa nevne spesifikke simulatorer er for detaljert for abstracts? to compute spikes, LFP signals and EEG signals generated by neurons and neuronal populations.

Keywords: extracellular potentials, LFP, EEG, ECoG, electrodiffusion, neuronal simulation

Contents

*correspondence: gaute.einevoll@nmbu.no

1. Introduction

Arguably, most of what we have learned about the mechanisms by which neurons and networks operate in living brains comes from recordings of extracellular potentials. In such recordings, electrical potentials are measured by electrodes that are either placed between cells in brain tissue (spikes, LFPs), at the cortical surface (ECoG, electrocorticography), or at the scalp (EEG, electroencephalograpy) (Figure 1). Spikes, the high-frequency part of the extracellular potentials recorded inside gray matter, are reliable signatures of neuronal action potentials, and spike measurements have been instrumental in mapping out, for example, receptive fields accounting for how sensory stimuli are represented in the brain. The analysis of the LFP signal, the low-frequency part of electrical potentials recorded inside gray matter, as well as the ECoG, and EEG signals is less straightforward. Interpretation of the signal in terms of the underlying neural activity has been difficult, and most analysis of the data has been purely statistical [Nunez and Srinivasan, 2006; Buzsáki et al., 2012; Einevoll et al., 2013a; Ilmoniemi and Sarvas, 2019].

The tradition of physics is different. Here candidate hypotheses are typically formulated as specific mathematical models, and predictions computed from the models are compared with experiments. In neuroscience this approach has been used to model activity in individual neurons using, for example, biophysically detailed neuron models based on the cable equation formalism (see, e.g., Koch [1999]; Sterratt et al. [2011]). Here the models have largely been developed and tested by comparison with membrane potentials recorded by intracellular electrodes in *in vitro* settings (but see Gold et al. [2007]). To pursue this mechanistic approach to network models in layered structures such as cortex or hippocampus, one would like to compare model predictions with all available experimental data, that is, not only spike times recorded for a small subset of the neurons, but also population measures such as LFP, ECoG and EEG signals [Einevoll et al., 2019]. This chapter addresses how to model such electrical population signals from neuron and network models.

In addition to allowing for validation on large-scale network models mimicking specific biological networks, e.g., Reimann et al. [2013]; Markram et al. [2015]; Billeh et al. [2020], we believe a key application is to generate model-based benchmarking data for validation of data analysis methods [Denker et al., 2012]. One example is the use of such benchmarking data to develop and test spike-sorting methods Hagen et al. [2016]; Buccino and Einevoll [2019] or test methods for localization and classification of cell types [Delgado Ruz and Schultz, 2014; Buccino et al., 2018]. Another example is testing of methods for analysis of LFP signals, such as CSD analysis [Pettersen et al., 2008; Łęski et al., 2011; Ness et al., 2015] or ICA analysis [Głąbska et al., 2014], or joint analysis of spike and LFP signals such as laminar population analysis (LPA) [Głąbska et al., 2016].

The standard way to compute extracellular potentials from neural activity is a two-step process [Holt and Koch, 1999; Lindén et al., 2014; Hagen et al., 2018]:

1. Compute the net transmembrane current in all neuronal segments in (networks of) biophysically-detailed neuron models, and
2. use volume-conductor (VC) theory to compute extracellular potentials from the these computed transmembrane currents.

This book chapter describes the origin of VC theory, that is, how it can be derived from a more detailed electrodiffusive theory describing dynamics of ions in the extracellular media. It also provides examples where our tool LFPy (`LFPy.github.io`) [Lindén et al., 2014; Hagen et al., 2018] is used to compute spikes, LFP signals and EEG signals generated by neurons and neuronal populations.

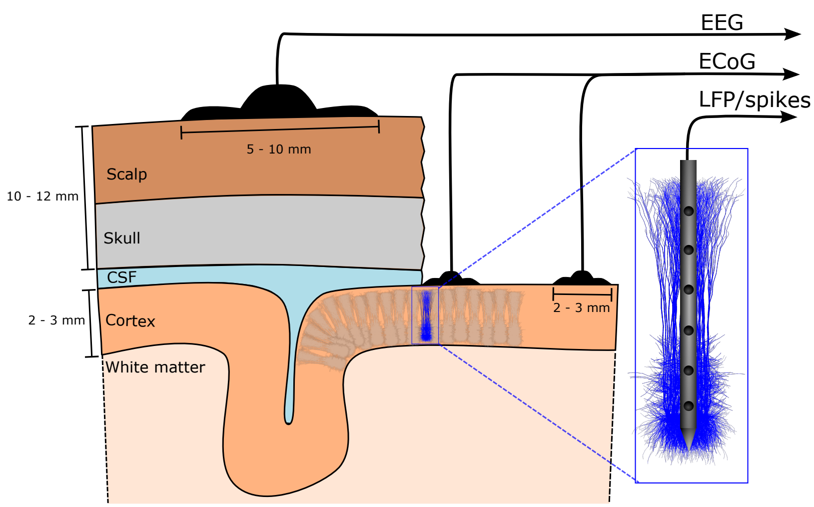

Figure 1: **LFP, ECoG and EEG.** The same basic building blocks, that is, currents caused by large numbers of synaptic input are contributing to several different measurable signals.

2. From electrodiffusion to volume conductor theory

The recorded extracellular potentials are generated by electrical currents, that is, movement of ions, in the extracellular space. Such an extracellular electrical current can in principle include several components:

1. a drift component (ions migrating in electrical fields),
2. a diffusion component (ions diffusing due to concentration gradients),
3. an advective component (extracellular fluid flow drags ions along), and
4. a displacement component (ions pile up and changes the local charge density).

Since the extracellular bulk fluid has very fast relaxation times and is very close to electroneutral, the latter two current components (3-4) are extremely small and are typically neglected [Grodzinsky, 2011; Gratiy et al., 2017]. The diffusive component (2) is acknowledged to play an important role for voltage dynamics on a tiny spatial scale, such as in synaptic clefts or in the close vicinity of neuronal membranes, where ion concentrations can change dramatically within very short times [Savtchenko et al., 2017; Pods, 2017]. At macroscopic tissue level, it is commonly believed that the diffusive current is much smaller than the drift current, so that even diffusive currents are typically neglected so that only the drift component (1) is considered. Then the extracellular medium is considered to be a volume conductor (VC) which greatly simplifies the calculation of extracellular potentials [Holt and Koch, 1999; Lindén et al., 2014].

However, if large ion-concentration gradients are present, diffusive currents could in principle affect measurable extracellular potentials [Halnes et al., 2016, 2017; Solbrå et al., 2018]. Thus in scenarios involving dramatic shifts in extracellular concentrations, such as spreading depression and related pathologies, diffusive effects are likely to be of key importance for shaping the extracellular potential [Almeida et al., 2004; O'Connell and Mori, 2016]. If so, VC theory is insufficient, and computationally much more expensive electrodiffusive modeling must be used instead.

In this section we start with a very general assumption of how ions moving through the brain under the combined influence of electric fields and concentration gradients TVN: strange sentence? . Building on this, we then first describe several computational schemes for modelling electrodiffusive processes before we derive the fundamental equations for VC theory assuming negligible effects from diffusion.

2.1. Ion concentration dynamics

The movement of ions, that is, charged atoms or molecules, in the brain are described in terms of the flux, and there are essentially two different processes that cause ions to move in the brain, namely diffusion and electrical drift. In such electrodiffusive processes, the flux density of an ion species k is given by [Koch, 1999]:

$$\mathbf{j_k} = -D_k \nabla c_k - \frac{D_k z_k c_k}{\psi} \nabla \phi, \tag{1}$$

where the first term on the right is Fick's law for the diffusive flux density j_k^{diff}, and the second term is the drift flux density j_k^{drift}, which expands Fick's law in the case where the diffusing particles also move due to electrostatic forces with a mobility D_k/ψ (cf. the Einstein-relation, Mori et al. [2008]). Here D_k is the diffusion coefficient of ion species k, ϕ is the electric potential, z_k is the valency of ion species k, and $\psi = RT/F$ is defined by the gas constant (R), Faraday's constant (F) and the temperature (T). The ion concentration dynamics of a given species is then given by the Nernst-Planck continuity equation:

$$\frac{\partial c_k}{\partial t} = -\nabla \cdot \mathbf{j_k} + f_k = \nabla \cdot \left[D_k \nabla c_k + \frac{D_k z_k c_k}{\psi} \nabla \phi \right] + f_k \tag{2}$$

where f_k represents any source term in the system, such as e.g., an ionic transmembrane current source [Solbrå et al., 2018].

In order the solve a set (i.e., one for each ion species present) of equations like eq. 2, one needs an expression for the electrical potential ϕ. There are two main approaches to this. The physically most detailed approach is to use the Poisson-Nernst-Planck (PNP) formalism [Léonetti and Dubois-Violette, 1998; Léonetti et al., 2004; Lu et al., 2007; Lopreore et al., 2008; Nanninga, 2008; Pods et al., 2013; Gardner et al., 2015]. Then ϕ is determined from Poisson's equation from electrostatics,

$$\nabla^2 \phi = -\rho/\epsilon, \tag{3}$$

where ϵ is the permittivity of the system, and ρ is the charge density associated with the ionic concentrations, as given by:

$$\rho = F \sum_k z_k c_k. \tag{4}$$

An alternative, more computationally efficient approach is to replace the Poisson equation with the simplifying approximation that the bulk solution is electroneutral [Mori et al., 2008; Mori, 2009; Mori and Peskin, 2009; Mori et al., 2011; Halnes et al., 2015, 2013; Pods, 2017; Niederer, 2013; O'Connell and Mori, 2016; Solbrå et al., 2018; Ellingsrud et al., 2020], which is a good approximation on spatiotemporal scales larger than micrometers and microseconds [Grodzinsky, 2011; Pods, 2017; Solbrå et al., 2018].

Both the PNP formalism and the electroneutral formalism allow us to compute the dynamics of ion concentrations and the electrical potential in the extracellular space of neural tissue containing an arbitrary set of neuronal and glial current sources. For example, in recent work, a version of the electroneutral formalism called the Kirchhoff-Nernst-Planck (KNP) formalism was developed into a framework for computing the extracellular dynamics (of c_k and ϕ) in a 3D space surrounding morphologically complex neurons simulated with the NEURON simulation tool [Solbrå et al., 2018]. However, both the PNP and electroneutral formalisms such as KNP keep track of the spatial distribution of ion concentrations, and as such they require a suitable meshing of the 3D space, and numerical solutions based on finite difference- or finite element methods. In both cases, simulations can become very heavy, and for systems at a tissue level the required computational demand may be too large to be feasible. For that reason, there is much to gain from deriving a simpler framework where effects of ion concentration dynamics are neglected, since, for many scenarios, this may be a good approximation. Below, we will derive this simpler frameworks, i.e., the standard volume conductor (VC) theory, using the Nernst-Planck fluxes (eq. 1) as a starting point.

2.2. Electrodynamics

If we multiply eq. 1 by $F \cdot z_k$ and take the sum over all ion species, we get an expression for the net electrical current density due to all particle fluxes:

$$\mathbf{i} = -\sum_k F z_k D_k \nabla c_k - \sigma \nabla \phi \tag{5}$$

where the first term is the diffusive current density i^{diff} and the second term is the drift current density i^{drift}. We have here identified the conductivity σ of the medium as [Koch, 1999]:

$$\sigma = F \sum_k \frac{\tilde{D}_k z_k^2}{\psi} c_k. \tag{6}$$

Current conservation in the extracellular space implies that:

$$\nabla \cdot \mathbf{i} = -\sum_k F z_k D_k \nabla^2 c_k - \nabla \cdot (\sigma \nabla \phi) = -C, \tag{7}$$

where C denotes the current source density (CSD), reflecting e.g., local neuronal or glial transmembrane currents. We note that this is essentially equivalent to eq. 2 at the level of single ion species, with the exception that eq. 2 contains a term $\partial c_k/\partial t$ for accumulation of ion species k, while eq. 7 does *not* contain a corresponding term $(\partial \rho/\partial t)$ for charge accumulation. Hence, in eq. 7 it is implicitly assumed that the extracellular bulk solution is electroneutral [Solbrå et al., 2018]. We note that in general, the CSD term includes both ionic transmembrane currents and transmembrane capacitive currents, and that the latter means that the local charge accumulation building up the transmembrane potential still occurs in the membrane Debye-layer.

Note that if we assume all concentrations to be constant in space, the diffusive term vanishes, and eq. 7 reduces to:

$$\nabla \cdot (\sigma \nabla \phi) = -C. \tag{8}$$

This the standard expression used in CSD theory [Mitzdorf, 1985; Nicholson and Freeman, 1975; Pettersen et al., 2006], where spatially distributed recordings of ϕ are used to make theoretical predictions of underlying current sources. When using eq. 8, it is implicitly assumed that the Laplacian of ϕ exclusively reflects transmembrane current sources, and that it is not contributed to by diffusive processes.

We note there are two conventions for defining the variables in eqns. 1-8, both of which are in use. The variables can be defined either relative to a tissue reference volume or relative to an extracellular reference volume. The former convention is the common convention used in volume conductor theory. Then concentrations denote the number of extracellular ions per unit tissue volume, sources denote the number of ions/the net charge per unit tissue volume per second, and flux/current densities are defined per unit tissue cross-section area. Then, σ interprets as the conductivity experienced by the current density per tissue cross section area.

As eq. 7 indicates, also diffusive processes can in principle contribute to the Laplacian of ϕ, and if present, they could give rise to a non-zero Laplacian of ϕ even in the absence of neuronal sources ($C = 0$). Previous computational studies have predicted that effects of diffusion on extracellular potentials are not necessarily small, but tend to be very slow, meaning that they will only affect the very low-frequency components of ϕ [Halnes et al., 2016, 2017]. This is due to the diffusive current being a direct function of ion concentrations c_k, which on a large spatial scale typically vary on a much slower time scale (seconds-minutes) than the fluctuations in ϕ that we commonly are interested in (milliseconds-seconds). Furthermore, electrodes used to record ϕ typically have a lower cutoff frequency of 0.1-1 Hz [Einevoll et al., 2013a], which means that most of the tentative diffusive contribution will be filtered out from experimental recordings. It may therefore be a good approximation to neglect the diffusive term, except in the case of pathologically dramatic concentration variations. For the rest of this chapter, we shall do so, and assume that electrodynamics in neural tissue can be determined by eq. 8.

2.3. Volume conductor theory

In simulations of morphologically complex neurons, we typically compute a set of transmembrane current sources for each neuronal segment [Koch, 1999]. Commonly, one assumes that the extracellular potential does not affect the neurons (i.e., no ephaptic coupling), since extracellular potentials are typically much smaller than the membrane potential of ∼-70 mV. By assuming that the tissue medium can be approximated as a volume conductor [Holt and Koch, 1999; Lindén et al., 2014], one can then use the standard CSD equation (eq. 8) to perform a forward modeling of the extracellular potential at each point in space surrounding the neuron(s).

If we consider the simple case of a single point-current source I_1 at the origin in an isotropic medium, the current density $\mathbf{i} = -\sigma\nabla\phi$ through a spherical shell with area $4\pi r^2$ must, due to the spherical symmetry, equal $I_1/4\pi r^2\ \hat{\mathbf{r}}$. Integration with respect to r gives us:

$$\phi = \frac{I_1}{4\pi\sigma r}, \tag{9}$$

where r is the distance from the source.

If we have several point-current sources, $I_1, I_2, I_3, ...$, in locations $\mathbf{r}_1, \mathbf{r}_2, \mathbf{r}_3 ...$, their contributions add up due to the linearity assumption (see sec. 2.3.2), and the potential in a point $\mathbf{r}$ is given by:

$$\phi(\mathbf{r}) = \frac{I_1}{4\pi\sigma|\mathbf{r}-\mathbf{r}_1|} + \frac{I_2}{4\pi\sigma|\mathbf{r}-\mathbf{r}_2|} + \frac{I_3}{4\pi\sigma|\mathbf{r}-\mathbf{r}_3|} + ... = \sum_k \frac{I_k}{4\pi\sigma|\mathbf{r}-\mathbf{r}_k|}. \tag{10}$$

Eq. 10 is often referred to as the point-source approximation [Holt and Koch, 1999; Lindén et al., 2014], since the membrane current from a neuronal segment is assumed to enter the extracellular medium in a single point. An often used further development is obtained by integrating eq. 10 along the segment axis, corresponding to the transmembrane current being evenly distributed along the segment axis, giving the line-source approximation [Holt and Koch, 1999; Lindén et al., 2014].

2.3.1. Current-dipole approximation

When estimating the extracellular potential far away from a volume containing a combination of current sinks and sources, it can often be useful to express eq. (10) in terms of a multipole expansion. That is, ϕ can be precisely described by [Nunez and Srinivasan, 2006],

$$\phi(R) = \frac{C_{\text{monopole}}}{R} + \frac{C_{\text{dipole}}}{R^2} + \frac{C_{\text{quadrupole}}}{R^3} + \frac{C_{\text{octupole}}}{R^4} + ..., \tag{11}$$

when the distance R from the center of the volume to the measurement point is larger than the distance from volume center to the most peripheral source [Jackson, 1998].

In neural tissue, there will be no current monopole contribution to the extracellular potential, that is, $C_{\text{monopole}} = 0$. This follows from the requirement inherent in the cable equation that the sum over all transmembrane currents, including the capacitive currents, across the neuronal surface has to be zero at all points in time [Pettersen et al., 2012]. Further, the quadrupole, octupole and higher-order contributions decay rapidly with distance R. Consequently, the multipole expansion can be approximated by the dipole contribution for large distances, a simplification known as the current-dipole approximation [Nunez and Srinivasan, 2006]:

$$\phi(\mathbf{R}) \approx \frac{C_{\text{dipole}}}{R^2} = \frac{1}{4\pi\sigma}\frac{|\mathbf{p}|\cos\theta}{R^2}. \tag{12}$$

Here, $\mathbf{p}$ is the current dipole moment and θ is the angle between the current dipole moment and the distance vector $\mathbf{R}$. The current dipole moment can be found by summing up all the position-weighted transmembrane currents from a neuron [Pettersen et al., 2008, 2014; Nunez and Srinivasan, 2006]:

$$\mathbf{p} = \sum_{k=1}^{N} I_k \mathbf{r}_k. \tag{13}$$

In the case of a two-compartment neuron model (see Section 3) with a current sink $-I$ at location $\mathbf{r}_1$ and a current source I at location $\mathbf{r}_2$, the current dipole moment can be formulated as $\mathbf{p} = -I\mathbf{r}_1 + I\mathbf{r}_2 = I(\mathbf{r}_2 - \mathbf{r}_1) = I\mathbf{d}$, where $\mathbf{d}$ is the distance vector between the current sink and the current source, giving the dipole length d and direction of the current dipole. The current-dipole approximation is applicable in the far-field limit, that is when R is much larger than the dipole length. For an investigation of the applicability of this approximation for the LFP generated by a single neuron, see Lindén et al. [2010].

2.3.2. Assumptions in volume conductor theory

The point-source approximation, eq. 10 (or the line-source version of it), and the current-dipole approximation, eq. (12), represent volume conductor theory in its simplest form, and are based on a set of assumptions, some of which may be relaxed for problems where it is relevant:

1. **Quasi-static approximation of Maxwell's equations:** Terms with time derivatives of the electrical and magnetic fields are neglected. This approximation appears to be well-justified for the relatively low frequencies relevant for brain signals, below about 10 kHz [Nunez and Srinivasan, 2006].
2. **Linear extracellular medium:** Linear relationship ($\mathbf{i} = -\sigma\nabla\phi$) between the current density $\mathbf{i}$ and the electrical field, $\nabla\phi$. This is essentially Ohm's law for volume conductors, and the relation is constitutive, meaning that it is observed in nature rather than derived from any physical principle [Nunez and Srinivasan, 2006; Pettersen et al., 2012].
3. **Frequency-independent conductivity:** Capacitive effects in neural tissue are assumed to be negligible compared to resistive effects in volume conduction. This approximation seems to be justified for the relevant frequencies in extracellular recordings [Logothetis et al., 2007; Miceli et al., 2017; Ranta et al., 2017], see Fig. 2. Note that it is possible to expand the formalism to include a frequency-dependent conductivity [Tracey and Williams, 2011; Miceli et al., 2017].
4. **Isotropic conductivity:** The electrical conductivity, σ, is assumed to be the same in all spatial directions. Cortical measurements have indeed found the conductivities to be comparable across different lateral directions in cortical grey matter [Logothetis et al., 2007]. However, the conductivity in the depth direction, i.e., parallel to the long apical dendrites, was found to be up to 50% larger than in the lateral direction in rat barrel cortex [Goto et al., 2010]. Anisotropic electrical conductivities have also been found in other brain regions, for example in frog cerebellum [Nicholson and Freeman, 1975] and in guinea-pig hippocampus [Holsheimer, 1987]. The approximation that σ is homogeneous is still often acceptable, as it normally gives fairly good estimations of the extracellular potential, at least in cortical tissue [Ness et al., 2015]. However, it is relatively straightforward to expand the formalism to account for anisotropic conductivities [Ness et al., 2015].
5. **Homogeneous conductivity:** The extracellular medium was assumed to have the same conductivity everywhere. Although neural tissue is highly non-homogeneous on the micrometer scale [Nicholson and Syková, 1998], microscale inhomogeneities may average out on a larger spatial scale, and a homogeneous conductivity seems to be a reasonable approximation within cortex [Logothetis et al., 2007]. In hippocampus, however, the conductivity has been found to be layer-specific [López-Aguado et al., 2001]. In situations where the assumption of a

homogeneous conductivity is not applicable, eq. 8 can always be solved for arbitrarily complex geometries using numerical methods, like the Finite Element Method (FEM) [Logg et al., 2012]. For some example neuroscience applications, see Moffitt and McIntyre [2005]; Frey et al. [2009]; Joucla and Yvert [2012]; Haufe et al. [2015]; Ness et al. [2015]; Buccino et al. [2019]; Obien et al. [2019]. For some simple non-homogeneous cases analytical solutions can still be obtained, for example through the Method of Images for *in vitro* brain slices [Ness et al., 2015], and the four-sphere head model for EEG signals (Sec. 5) [Næss et al., 2017].

6. **No effects from ion diffusion:** To account for diffusion of ions, one would need to compute the electrodynamics of the system using one of the electrodiffusive frameworks presented in Section 2.1.

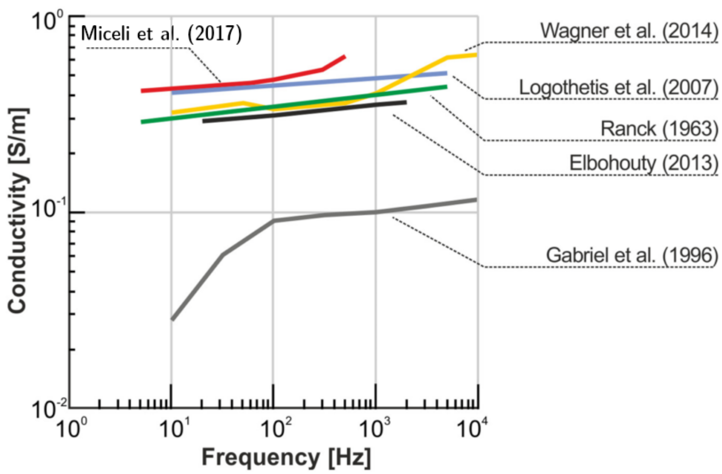

Figure 2: **Literature review of reported conductivities in various species and experimental setups.** Most studies seem to indicate a very weak frequency dependence of the extracellular conductivity, which would have a negligible effect on measured extracellular potentials [Miceli et al., 2017]. The very low and strongly frequency dependent values measured by Gabriel et al. [1996] represents an outlier, and although it has received substantial attention, it has to the best of our knowledge not been reproduced by any other study. For details about the data, see [Miceli et al., 2017], and references therein [Ranck, 1963; Gabriel et al., 1996; Logothetis et al., 2007; Elbohouty, 2013; Wagner et al., 2014].

Volume conductor theory is the fundament for forward modeling of extracellular potentials at different spatial scales, from extracellular spikes, LFPs and MUAs, to ECoGs and EEGs. In the following sections we shall review previous modeling works, and insights from simulating electrical potentials at these different scales. We use the software LFPy [Lindén et al., 2014; Hagen et al., 2018, 2019], which has volume conductor theory incorporated and can in principle be used to compute extracellular potentials on arbitrarily large spatial scales, surrounding arbitrarily large neuronal populations.

2.4. Modeling electrodes

The simplest and most commonly used approach when modeling extracellular recordings is to calculate the extracellular potential at single points following one of the approaches outlined above, and use this as a measure of recorded potentials. Implicitly, this assumes ideal point electrodes, that is, that the electrodes (and electrode shank) do not affect the extracellular potential and that the extracellular potential does not vary substantially over the surface of the electrodes. (This point-electrode assumption was used for all simulation examples in this chapter).

A numerically straightforward extension is the disc-electrode approximation where the potential is evaluated at a number of points on the electrode surface, and the average calculated [Nunez and Srinivasan, 2006; Lindén et al., 2014]. GTE: Does Nunez talk about this? TVN: Yes, eq. (5.30) in the book, however, strangely they actually use a volume integral, so maybe just remove the reference? This approach takes into account the physical extent of the electrode, but not any effect the electrode itself might have on the electric potential. Close to the electrode surface the electric potential will however be affected by the presence of the high-conductivity electrode contact [McIntyre and Grill, 2001; Moulin et al., 2008], and a third, and numerically much more comprehensive approach to modeling electrodes is to use the Finite Element Method (FEM) to model the electrode [Moulin et al., 2008; Ness et al., 2015], or the electrode shank [Moffitt and McIntyre, 2005; Buccino et al., 2019]. Using FEM for validation, Ness et al. [2015] found that the ideal point-electrode and disc-electrode approximations where reasonably accurate when the distance between the current sources and the recording electrode was bigger than $\sim$4 times and $\sim$2 times the electrode radius, respectively, indicating that the effects of the electrodes themselves are negligible in most cases [Nelson and Pouget, 2010]. The presence of large multi-contact electrode probes can, however, substantially affect the extracellular potential in its vicinity, by effectively introducing a large non-conducting volume [Mechler and Victor, 2012], and this can amplify or dampen recorded potentials from nearby cells by almost a factor of two, depending on whether the cell is in front of or behind the electrode shank [Buccino et al., 2019].

Note that for modelling current stimulation electrodes (as opposed to just recording electrodes), more complex electrode models might be needed due to electrode polarization effects [McIntyre and Grill, 2001; Martinsen and Grimnes, 2008; Joucla and Yvert, 2012].

3. Single-cell contributions to extracellular potentials

The transmembrane currents of a neuron during any neural activity can be used to calculate extracellular potentials, by applying the formalism described in Sec. 2.3, and in the simplest case eq. 10. Current conservation requires that the transmembrane currents across the entire cellular membrane at any given time sum to zero [Koch, 1999; Nunez and Srinivasan, 2006], and since an excitatory synaptic input generates a current sink (negative current), this will necessarily lead to current sources elsewhere on the cell. This implies that point neurons, that is, neurons with no spatial structure, will have no net transmembrane currents, and hence cause no extracellular potentials (Fig. 3A). The simplest neuron models that are capable of producing extracellular potentials are therefore two-compartment models, which will have two equal but opposite transmembrane currents, giving rise to perfectly symmetric extracellular potentials (Fig. 3B).

Multi-compartment neuron models mimicking the complex spatial structure of real neurons will typically give rise to complicated patterns of current sinks and sources (negative and positive currents respectively), leading to complex, but mostly dipolar-like extracellular potentials (Fig. 3C) [Einevoll et al., 2013a]. Note that this framework for calculating extracellular potentials is valid both for subthreshold and suprathreshold neural activity, that is, when a cell receives synaptic input that does not trigger, or does trigger an action potential, respectively (Fig. 3, D versus E).

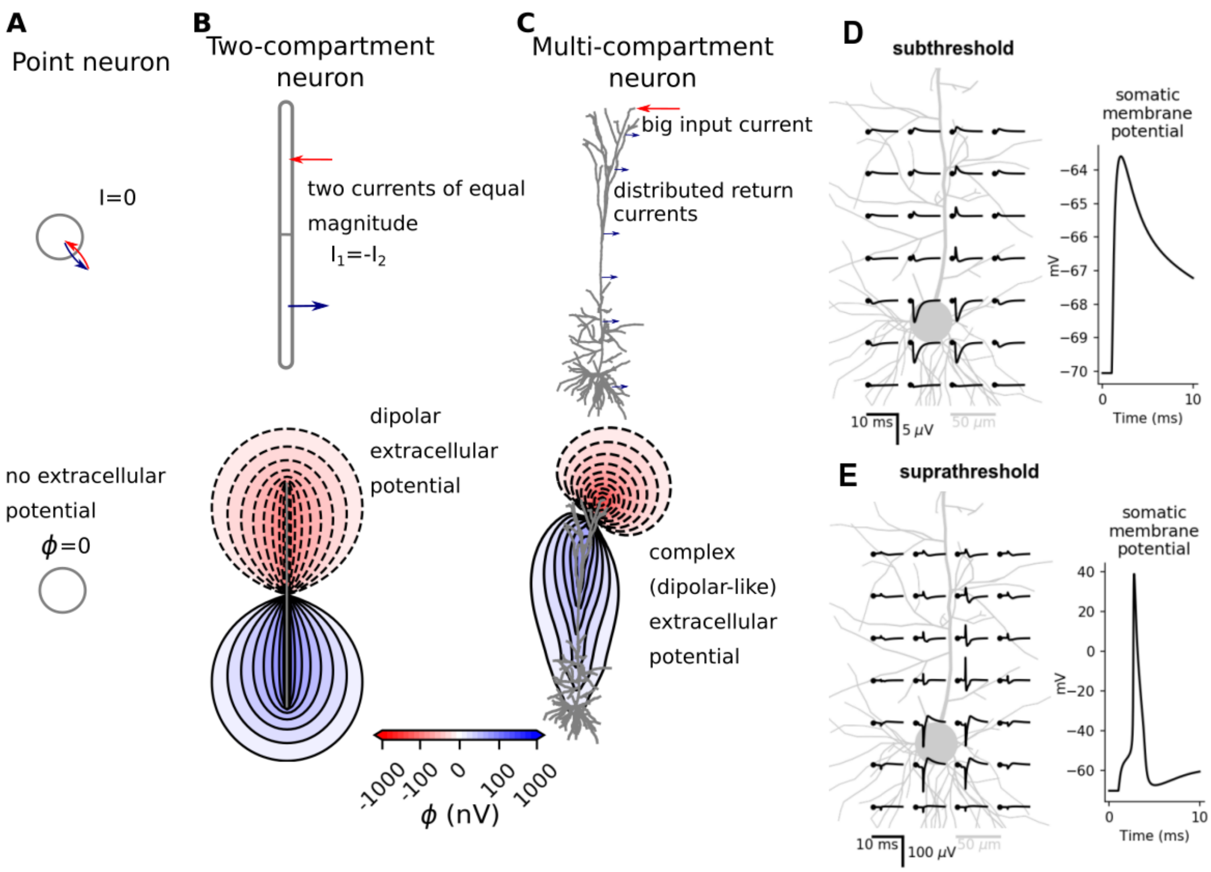

Figure 3: **Single-cell contributions to the extracellular potential.** **A**: Point neurons have no net currents (top), and therefore cause no extracellular potentials (bottom). **B**: Two-compartment neuron models have two opposite currents of identical magnitude (top), and cause perfectly symmetric dipolar-like extracellular potentials (bottom). **C**: Multi-compartment neuron models [Hay et al., 2011] give rise to complex source-sink patterns (top) and complex (but mostly dipolar-like) extracellular potentials (bottom). **D, E**: A single somatic synaptic input to a complex multi-compartment cell model, either subthreshold (D) or suprathreshold (E; double synaptic weight of D), illustrating that the same framework can be used to calculate both the LFP contribution from subthreshold synaptic input, and extracellular action potentials.

4. Intra-cortical extracellular potentials from neural populations

Extracellular potentials measured within neural tissue are often split into two separate frequency domains, which reflect different aspects of the underlying neural activity. The low frequency part, that is, the local field potential (LFP), is thought to mostly reflect synaptic input to populations of pyramidal cells, while the high-frequency part, that is, the multi-unit activity (MUA), reflects the population spiking activity (Fig. 4).

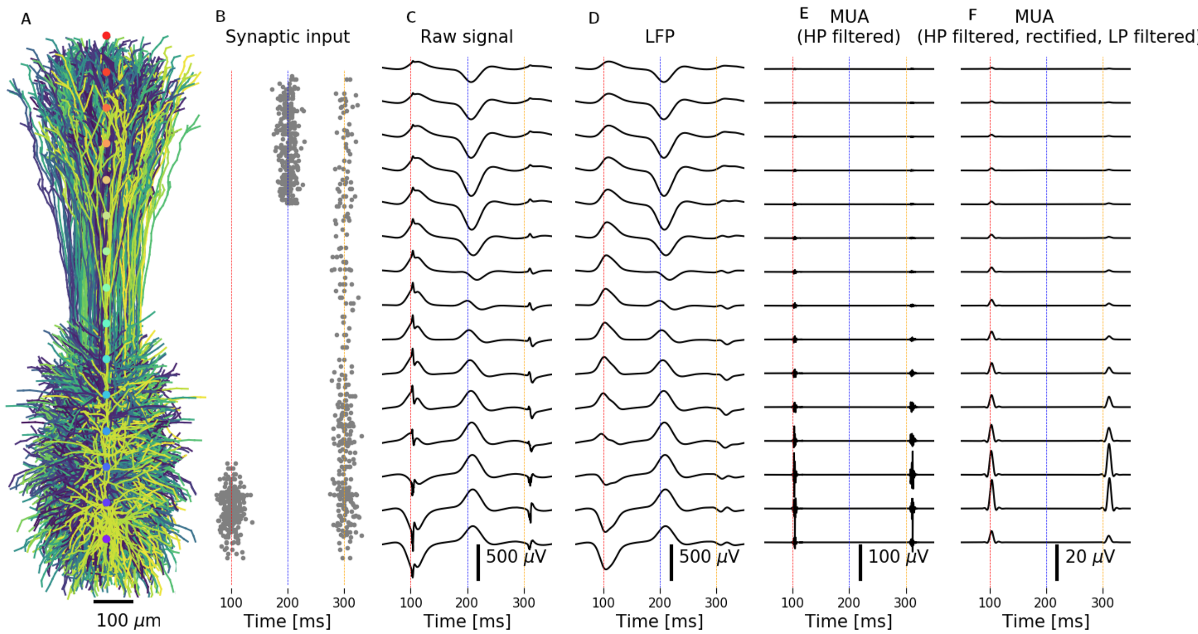

Figure 4: **Extracellular potentials from different waves of synaptic input**. Different brain signals from separate waves of synaptic input to 10 000 layer 5 pyramidal cells from rat [Hay et al., 2011]. **A**: A subset of 100 pyramidal cells, with the LFP electrode locations indicated in the center (colored dots). **B**: Depth-resolved synaptic inputs arrive in three waves, first targeting the basal dendrites (t=100 ms), then the apical dendrites (t=200 ms), and lastly uniformly across the entire depth (t=300 ms). Note that all synaptic input is pre-defined, that is, there is no network activity. **C**: The extracellular potential at different depths (corresponding to dots in panel A), including both spikes and synaptic input. **D**: The LFP, that is, a low-pass filtered version of the raw signal in C. **E**: The MUA, that is, a high-pass filtered version of the raw signal in C. **F**: Another version of the MUA which is a rectified and low-pass filtered version of the MUA signal in E. All filters where 4th order Butterworth filters in forward-backward mode [NeuroEnsamble, 2017]. For illustration purposes a relatively low cut-off frequency of 50 Hz was chosen for the LFP low-pass filter. The MUA was first high-pass filtered above 300 Hz (E and F), then rectified and low-pass filtered below 300 Hz (F).

4.1. Local field potentials

The LFP is the low-frequency part ($\lesssim$ 500 Hz) of the extracellular potentials, and it is among the oldest and most used brain signals in neuroscience [Einevoll et al., 2013a]. The LFP is expected to be dominated by synaptic inputs asymmetrically placed onto populations of geometrically aligned neurons [Nunez and Srinivasan, 2006; Lindén et al., 2011; Einevoll et al., 2013b]. In cortex and hippocampus, neurons can broadly speaking be divided into two main classes: the inhibitory interneurons, and the excitatory pyramidal neurons. Pyramidal neurons typically have a clear axis of orientation, that is, the apical dendrites of close-by pyramidal neurons tend to be oriented in the same direction (Fig. 4A). This geometrical alignment is important because the LFP contributions from the individual pyramidal cells also align and therefore sum constructively. For example, basal excitatory synaptic input (Fig. 4B, time marked by red line) generates a current sink and corresponding negative LFP deflection in the basal region, and simultaneously a current source and corresponding positive LFP deflection in the apical region (Fig. 4D, time marked by red line), while apical excitatory synaptic input leads to the reversed pattern (Fig. 4B,D, time marked by blue line). Importantly, this means that excitatory input that simultaneously targets both the apical and the basal dendrite will give opposite source/sink patterns which will lead to substantial cancellation and a weak LFP contribution (Fig. 4B, D, time marked by orange line). The same arguments also apply to inhibitory synaptic inputs, with the signs of the currents and LFPs reversed.

Note that, for example, the LFP signature of apical excitatory synaptic input is inherently similar to that of basal inhibitory input, and indeed, separating between cases like this pose a real challenge in interpreting LFP signals [Lindén et al., 2010].

In contrast to pyramidal neurons, interneurons often lack any clear orientational specificity, meaning that the current dipoles from individual interneurons, which might by themselves be sizable [Lindén et al., 2010], do not align, leading to negligible net contributions to LFP signals [Mazzoni et al., 2015]. Note, however, that the interneurons may indirectly cause large LFP contributions through their synaptic inputs onto pyramidal cells [Teleńczuk et al., 2017; Hagen et al., 2016].

It has been demonstrated that correlations among the synaptic inputs to pyramidal cells can amplify the LFP signal power by orders of magnitude, with the implication that populations receiving correlated synaptic input can dominate the LFP also 1-2 mm outside of the population [Lindén et al., 2011; Łęski et al., 2013].

Somatic action potentials lasting only a few milliseconds are generally expected to contribute little to cortical LFP signals [Pettersen et al., 2008; Pettersen and Einevoll, 2008; Einevoll et al., 2013a; Haider et al., 2016]: Their very short duration with both positive and negative phases (Fig. 3E) will typically give large signal cancellations of the contributions from individual neurons, and their high frequency content is to a large degree removed from LFPs during low-pass filtering. Note, however, that in the hippocampus the highly synchronized spikes found during sharp wave ripples are expected to also contribute to shaping of the LFP [Schomburg et al., 2012; Luo et al., 2018].

Other active conductances may contribute in shaping the LFP, for example, the slower dendritic calcium spikes [Suzuki and Larkum, 2017] or long-lasting after-hyperpolarization currents [Reimann et al., 2013]. Further, subthreshold active conductances can also shape the LFP by molding the transmembrane currents following synaptic input, and the hyperpolarization-activated cation channel I_h may play a key role in this, both through asymmetrically changing the membrane conductance, and by introducing apparent resonance peaks in the LFP [Ness et al., 2016, 2018].

4.2. MUA

While LFPs are thought to mainly reflect the synaptic input to large populations of pyramidal neurons, the multi-unit activity (MUA) can be used to probe the population spiking activity [Einevoll et al., 2007; Pettersen et al., 2008] (Fig. 4 E,F). In other words, the MUA holds complimentary information to the LFP. In particular, this can be useful for some cell-types, like stellate cells and inhibitory interneurons, which are expected to have very weak LFP contributions [Lindén et al., 2011], but might still be measurable through their spiking activity. Similarly, spatially uniformly distributed synaptic input to pyramidal neurons results in a negligible LFP contribution (Fig. 4C, time marked by orange line), while the population might still contribute substantially to the MUA through the extracellular action potentials (Fig. 4E-F, time marked by orange line).

5. ECoG and EEG

In order to measure electric potentials in the immediate vicinity of neurons, like LFP and MUA signals, we need to insert sharp electrodes into the brain. This highly invasive technique is quite common in animal studies, but can only be applied to humans when there is a clear medical need, for example in patients with intractable epilepsy [Zangiabadi et al., 2019]. However, electric potentials generated by neural activity extend beyond neural tissue and can also be measured outside the brain: Placing electrodes on the brain surface, as in electrocorticography (ECoG), is a technique that requires some surgery. With electroencephalography (EEG), on the other hand, potentials are measured non-invasively, directly on top of the scalp.

Since EEG electrodes are located relatively far away from the neuronal sources, the current dipole approximation, eq. (12), combined with some head model, can be applied for computing EEG signals [Nunez and Srinivasan, 2006; Ilmoniemi and Sarvas, 2019]. By collapsing the transmembrane currents of a neuron simulation into one single current dipole moment, see eq. (13), we can calculate EEG from arbitrary neural activity (Fig. 5). The current dipole approximation is however not unproblematic to use for computing ECoG signals, as the ECoG electrodes may be located too close to the signal sources for the approximation to apply, see Hagen et al. [2018].

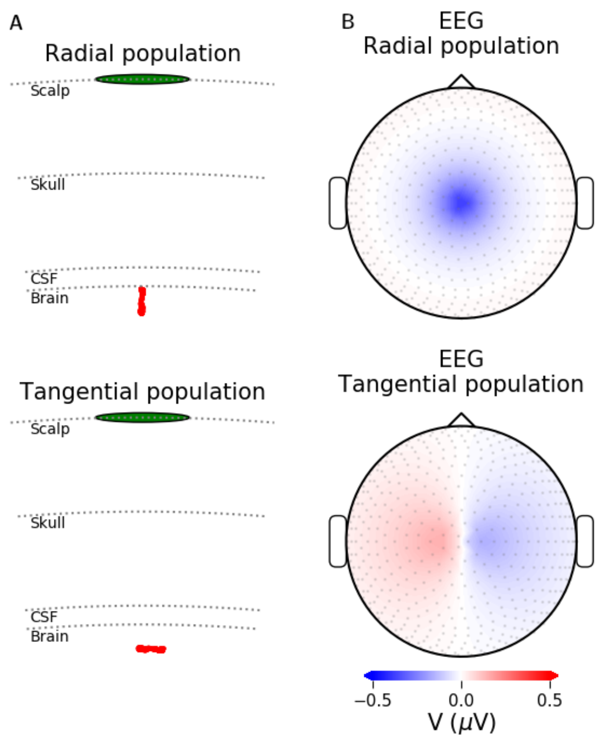

Figure 5: **EEG from apical synaptic input to population of pyramidal cells**. **A**: The four-sphere head model with two orientations of the neural population from Fig. 4, either radial, mimicking a population in a gyrus (top) or tangential, mimicking a population in a sulcus (bottom). **B**: A snapshot of the EEG signal at the head surface for apical input (time marked with blue dotted line in Fig. 4), for a radial population (top) or tangential population (bottom).

5.1. Head models

Electric potentials measured on the scalp surface will be affected by the geometries and conductivities of the different constituents of the head [Nunez and Srinivasan, 2006]. This can be incorporated in EEG calculations by applying simplified or more complex head models. A well-known simplified head model is the analytical four-sphere model, consisting of four concentric shells representing brain tissue, cerebrospinal fluid (CSF), skull and scalp, where the conductivity can be set individually for each shell [Næss et al., 2017; Srinivasan et al., 1998; Nunez and Srinivasan, 2006] (Fig. 6, Fig. 7A,B). More complex head models make use of high-resolution anatomical MRI-data to map out a geometrically detailed head volume conductor. The link between current dipoles in the brain and resulting EEG signals is determined applying numerical methods such as the finite element method [Larson and Bengzon, 2013; Logg et al., 2012]. Once this link is established we can in principle insert a dipole representing arbitrary neural activity into such a model, and compute the resulting EEG signals quite straightforwardly. The New York Head model is an example of one such pre-solved complex head model, see Fig. 7C,D [Huang et al., 2016].

The head models themselves introduce no essential frequency filtering of the EEG signal [Pfurtscheller and Cooper, 1975; Nunez and Srinivasan, 2006; Ranta et al., 2017], however, substantial spatial filtering will occur (Fig. 6). Additionally, the measured (or modeled) signals represent the average potential across the elecrode surface, and the large electrode sizes used in ECoG/EEG recordings can have important effect on the measured signals [Nunez and Srinivasan, 2006; Hagen et al., 2018; Dubey and Ray, 2019].

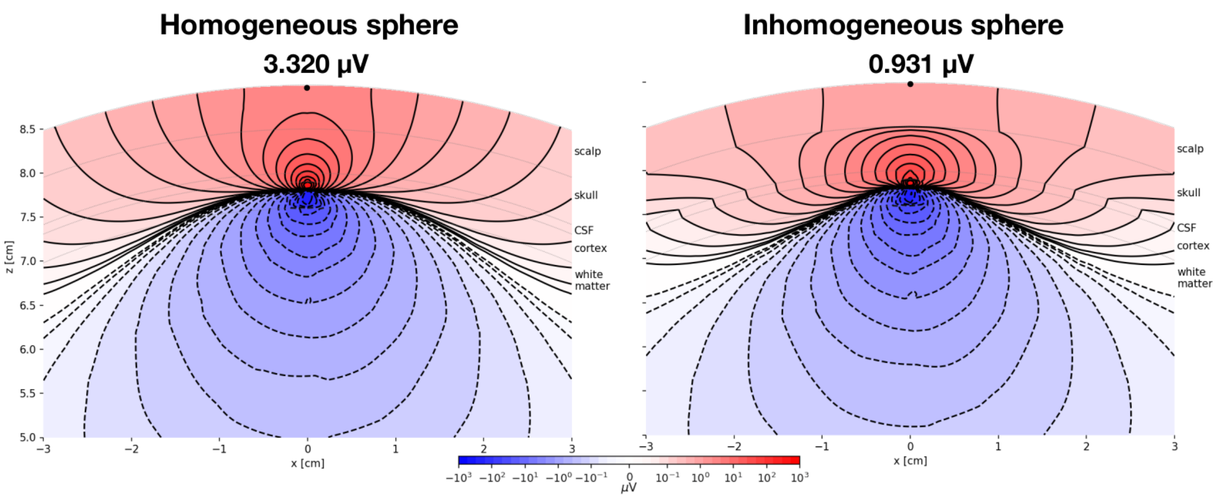

Figure 6: **Effect of head inhomogeneities**. The same current dipole will give substantially different potentials on the head surface if the different conductivities of the head is included in a FEM model [Næss et al., 2017]. Left: Homogeneous sphere, with electrical conductivity, $\sigma = 0.33$ S/m everywhere. Right: Standard four-sphere head model, with $\sigma_{\text{brain}} = 0.33$ S/m, $\sigma_{\text{CSF}} = 5\sigma_{\text{brain}}$, $\sigma_{\text{skull}} = \sigma_{\text{brain}}/20$, $\sigma_{\text{scalp}} = \sigma_{\text{brain}}$.

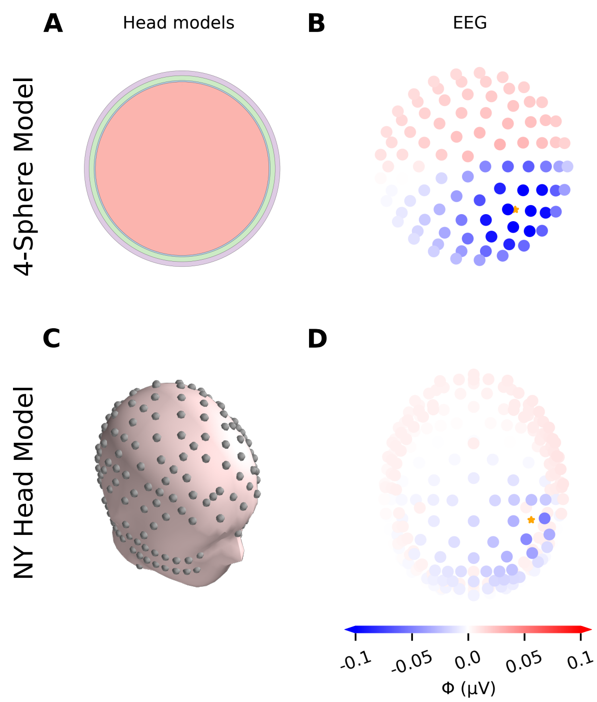

Figure 7: **The four-sphere head model and the NY Head model**. EEG signals from population dipole resulting from waves of synaptic input to 10 000 layer 5 pyramidal cells from rat [Hay et al., 2011]. **A**: The four-sphere model consisting of four concentrical shells: brain, CSF, skull and scalp. **B**: Maximum EEG signals (ϕ) on scalp surface electrodes resulting from population dipole placed at location marked by orange star, computed with the four-sphere model. **C**: Illustration of the New York Head model. **D**: EEG signals computed with the New York Head model, equivalent to panel **B**.

6. Discussion

In the present chapter we have derived and applied well-established biophysical forward-modeling schemes for computing extracellular electrical potentials recorded inside and outside the brain. These electrical potentials include spikes (both single-unit and multiunit activity (MUA)), LFP, ECoG and EEG signals. The obvious application of this scheme is computation of electrical signals from neuron and network activity for comparison with experiments so that candidate models can be tested [Einevoll et al., 2019] or inferred [Goncalves et al., 2019; Skaar et al., 2020]. Another key application is the computation of benchmarking data for testing of data analysis methods such as spike sorting or CSD analysis [Denker et al., 2012].

Inverse modeling of recorded electrical potentials, that is, estimation of the neural sources underlying the signals, is inherently an ill-posed problem. This means that no unique solution for the size and position of the sources exists. However, prior knowledge about the underlying sources and how they generate the recorded signals, can be used to increase the identifiability. For example, several methods for the estimation of so-called current-source density (CSD) from LFP recordings have been developed by building the present forward model into the CSD estimator [Pettersen et al., 2006; Potworowski et al., 2012; Cserpán et al., 2017].

The present chapter has focused on the modeling of measurements of extracellular electrical signals. Another important and related brain signal is the magnetic fields recorded outside the head in magnetoencephalograpy (MEG). These magnetic signals also stem from the transmembrane currents of neurons and, similar to EEG, the signal can be computed based on the current dipoles of the underlying neurons in cortex [Hämäläinen et al., 1993; Ilmoniemi and Sarvas, 2019]. The new version of our tool LFPy, which was used in generating the examples in the present chapter, thus also includes the ability to compute MEG signals [Hagen et al., 2018].

There are also other measurement modalities where detailed modeling could be pursued to allow for a more quantitative analysis of recorded data. Voltage-sensitive dye imaging (VSDI) reflects area-weighted neuronal membrane potentials [Chemla and Chavane, 2012], while two-photon calcium imaging measures the intracellular calcium dynamics [Helmchen, 2012]. Both are accessible through neuronal simulations of the type used to compute electrical and magnetic signals. Functional magnetic resonance imaging (fMRI) instead reflect blood dynamics [Bartels et al., 2012], which typically are not explicitly included in neural network models.

Acknowledgements

This research has received funding from the European Union Horizon 2020 Framework Programme for Research and Innovation under Specific Grant Agreement No. 785907 (Human Brain Project SGA2), and the Research Council of Norway (Notur, nn4661k; DigiBrain, no. 248828; INCF National Node, no. 269774).

Almeida, A. C. G., Texeira, H. Z., Duarte, M. A., Infantosi, A. F. C., March 2004. Modeling extracellular space electrodiffusion during lea/spl tilde/o's spreading depression. IEEE Transactions on Biomedical Engineering 51 (3), 450–458.

Bartels, A., Goense, J., Logothetis, N., Sep. 2012. Functional magnetic resonance imaging. In: Brette, R., Destexhe, A. (Eds.), Handbook of Neural Activity Measurement. Cambridge University Press, pp. 92–135.

Billeh, Y. N., Cai, B., Gratiy, S. L., Dai, K., Iyer, R., Gouwens, N. W., Abbasi-Asl, R., Jia, X., Siegle, J. H., Olsen, S. R., Koch, C., Mihalas, S., Arkhipov, A., 2020. Systematic integration of structural and functional data into multi-scale models of mouse primary visual cortex. Neuron.
URL https://www.biorxiv.org/content/early/2019/06/06/662189

Buccino, A. P., Einevoll, G. T., 2019. Mearec: a fast and customizable testbench simulator for ground-truth extracellular spiking activity. bioRxiv.
URL https://www.biorxiv.org/content/early/2019/07/03/691642

Buccino, A. P., Kordovan, M., Ness, T. V., Merkt, B., Häfliger, P. D., Fyhn, M., Cauwenberghs, G., Rotter, S., Einevoll, G. T., 2018. Combining biophysical modeling and deep learning for multi-electrode array neuron localization and classification. Journal of Neurophysiology 120, 1212–1232. URL http://www.ncbi.nlm.nih.gov/pubmed/29847231https://www.physiology.org/doi/10.1152/jn.00210.2018

Buccino, A. P., Kuchta, M., Jæger, K. H., Ness, T. V., Berthet, P., Mardal, K.-A., Cauwenberghs, G., Tveito, A., 2019. How does the presence of neural probes affect extracellular potentials? Journal of Neural Engineering 16 (2).

Buzsáki, G., Anastassiou, C. a., Koch, C., Jun. 2012. The origin of extracellular fields and currents–EEG, ECoG, LFP and spikes. Nature reviews. Neuroscience 13 (6), 407–20. URL http://www.ncbi.nlm.nih.gov/pubmed/22595786

Chemla, S., Chavane, F., Sep. 2012. Voltage-sensitive dye imaging. In: Brette, R., Destexhe, A. (Eds.), Handbook of Neural Activity Measurement. Cambridge University Press, pp. 92–135.

Cserpán, D., Meszéna, D., Wittner, L., Tóth, K., Ulbert, I., Somogyvári, Z., Wójcik, D. K., Nov. 2017. Revealing the distribution of transmembrane currents along the dendritic tree of a neuron from extracellular recordings. eLife 6.

Delgado Ruz, I., Schultz, S. R., 2014. Localising and classifying neurons from high density MEA recordings. Journal of Neuroscience Methods 233, 115–128. URL http://dx.doi.org/10.1016/j.jneumeth.2014.05.037

Denker, M., Einevoll, G., Franke, F., Grün, S., Hagen, E., Kerr, J., Nawrot, M., Ness, T. B., Wójcik, T. W. D., 2012. Report from 1st incf workshop on validation of analysis methods. Tech. rep., International Neuroinformatics Coordinating Facility (INCF).

Dubey, A., Ray, S., 2019. Cortical electrocorticogram (ecog) is a local signal. Journal of Neuroscience 39 (22), 4299–4311.

Einevoll, G., Kayser, C., Logothetis, N., Panzeri, S., 2013a. Modelling and analysis of local field potentials for studying the function of cortical circuits. Nature Reviews Neuroscience 14, 770–785.

Einevoll, G. T., Destexhe, A., Diesmann, M., Grün, S., Jirsa, V., de Kamps, M., Migliore, M., Ness, T. V., Plesser, H. E., Schürmann, F., 2019. The Scientific Case for Brain Simulations. Neuron 102 (4), 735–744.

Einevoll, G. T., Lindén, H., Tetzlaff, T., Łęski, S., Pettersen, K. H., 2013b. Local Field Potentials - Biophysical Origin and Analysis. In: Quiroga, R. Q., Panzeri, S. (Eds.), Principles of Neural Coding. CRC Press, Boca Raton, FL, Ch. 3, pp. 37–60.

Einevoll, G. T., Pettersen, K. H., Devor, A., Ulbert, I., Halgren, E., Dale, A. M., Mar. 2007. Laminar population analysis: estimating firing rates and evoked synaptic activity from multielectrode recordings in rat barrel cortex. Journal of neurophysiology 97 (3), 2174–90. URL http://www.ncbi.nlm.nih.gov/pubmed/17182911

Elbohouty, M., 2013. Electrical Conductivity of Brain Cortex Slices in Seizing and Non-seizing States. Ph.D. thesis, The University of Waikato.

Ellingsrud, A. J., Solbrå, A., Einevoll, G. T., Halnes, G., Rognes, M. E., 2020. Finite element simulation of ionic electrodiffusion in cellular geometries. Frontiers in Neuroinformatics 14, 11.
URL https://www.frontiersin.org/article/10.3389/fninf.2020.00011

Frey, U., Egert, U., Heer, F., Hafizovic, S., Hierlemann, a., mar 2009. Microelectronic system for high-resolution mapping of extracellular electric fields applied to brain slices. Biosensors & bioelectronics 24 (7), 2191–8.
URL http://www.ncbi.nlm.nih.gov/pubmed/19157842

Gabriel, S., Lau, R. W., Gabriel, C., nov 1996. The dielectric properties of biological tissues: II. Measurements in the frequency range 10 Hz to 20 GHz. Physics in medicine and biology 41 (11), 2251–69.
URL http://www.ncbi.nlm.nih.gov/pubmed/8938025

Gardner, C. L., Jones, J. R., Baer, S. M., Crook, S. M., Feb. 2015. Drift-diffusion simulation of the ephaptic effect in the triad synapse of the retina. Journal of computational neuroscience 38 (1), 129–42.
URL http://www.ncbi.nlm.nih.gov/pubmed/25260382

Gold, C., Henze, D. A., Koch, C., Aug 2007. Using extracellular action potential recordings to constrain compartmental models. J. Comput. Neurosci. 23 (1), 39–58.
URL http://dx.doi.org/10.1007/s10827-006-0018-2

Goncalves, P. J., Lueckmann, J.-M., Deistler, M., Nonnenmacher, M., Öcal, K., Bassetto, G., Chintaluri, C., Podlaski, W. F., Haddad, S. A., Vogels, T. P., Greenberg, D. S., Macke, J. H., 2019. Training deep neural density estimators to identify mechanistic models of neural dynamics. bioRxiv.

Goto, T., Hatanaka, R., Ogawa, T., Sumiyoshi, A., Riera, J., Kawashima, R., 2010. An evaluation of the conductivity profile in the somatosensory barrel cortex of wistar rats. Journal of neurophysiology 104 (6), 3388–3412.

Gratiy, S. L., Halnes, G., Denman, D., Hawrylycz, M. J., Koch, C., Einevoll, G. T., Anastassiou, C. A., 2017. From Maxwell's equations to the theory of current-source density analysis. European Journal of Neuroscience 45 (8), 1013–1023.

Grodzinsky, F., 2011. Fields, Forces, and Flows in Biological Systems. Garland Science, Taylor & Francis Group, London & New York.

Głąbska, H., Potworowski, J., Łęski, S., Wójcik, D. K., 2014. Independent components of neural activity carry information on individual populations. PLoS One 9 (8), e105071.
URL http://dx.doi.org/10.1371/journal.pone.0105071

Głąbska, H. T., Norheim, E., Devor, A., Dale, A. M., Einevoll, G. T., Wójcik, D. K., 2016. Generalized laminar population analysis (glpa) for interpretation of multielectrode data from cortex. Frontiers in neuroinformatics 10, 1.

Hagen, E., Dahmen, D., Stavrinou, M. L., Lindén, H., Tetzlaff, T., Van Albada, S. J., Grün, S., Diesmann, M., Einevoll, G. T., 2016. Hybrid scheme for modeling local field potentials from point-neuron networks. Cerebral Cortex 26 (12), 4461–4496.

Hagen, E., Næss, S., Ness, T. V., Einevoll, G. T., 2018. Multimodal modeling of neural network activity: computing LFP, ECoG, EEG and MEG signals with LFPy 2.0. Front Neuroinform 12 (92).

Hagen, E., Næss, S., Ness, T. V., Einevoll, G. T., 2019. LFPy – multimodal modeling of extracellular neuronal recordings in Python. In: Encyclopedia of Computational Neuroscience. Springer, New York, NY, p. 620286.
URL http://biorxiv.org/content/early/2019/05/03/620286.abstract

Haider, B., Schulz, D. P. A., Häusser, M., Carandini, M., 2016. Millisecond Coupling of Local Field Potentials to Synaptic Currents in the Awake Visual Cortex. Neuron 90, 35–42.

Halnes, G., Mäki-Marttunen, T., Keller, D., Pettersen, K. H., Andreassen, O. A., Einevoll, G. T., 2016. Effect of ionic diffusion on extracellular potentials in neural tissue. PLoS computational biology 12 (11), e1005193.

Halnes, G., Mäki-Marttunen, T., Pettersen, K. H., Andreassen, O. A., Einevoll, G. T., 2017. Ion diffusion may introduce spurious current sources in current-source density (CSD) analysis. Journal of Neurophysiology 118 (1), 114–120.
URL http://jn.physiology.org/lookup/doi/10.1152/jn.00976.2016

Halnes, G., Ø stby, I., Pettersen, K. H., Omholt, S. W., Einevoll, G. T., 2015. An Electrodiffusive Formalism for Ion Concentration Dynamics in Excitable Cells and the Extracellular Space Surrounding Them. In: Advances in cognitive neurodynamics (IV). Springer Netherlands, pp. 353–360.
URL http://link.springer.com/chapter/10.1007/978-94-017-9548-7_50

Halnes, G., Østby, I., Pettersen, K. H., Omholt, S. W., Einevoll, G. T., 2013. Electrodiffusive model for astrocytic and neuronal ion concentration dynamics. PLoS computational biology 9 (12), e1003386.

Hämäläinen, M., Hari, R., Ilmoniemi, R. J., Knuutila, J., Lounasmaa, O. V., 1993. Magnetoencephalography?theory, instrumentation, and applications to noninvasive studies of the working human brain. Reviews of modern Physics 65 (2), 413.

Haufe, S., Huang, Y., Parra, L. C., 2015. A highly detailed FEM volume conductor model based on the ICBM152 average head template for EEG source imaging and TCS targeting. Conference proceedings : ... Annual International Conference of the IEEE Engineering in Medicine and Biology Society. IEEE Engineering in Medicine and Biology Society. Annual Conference 2015, 5744–5747.

Hay, E., Hill, S., Schürmann, F., Markram, H., Segev, I., jul 2011. Models of neocortical layer 5b pyramidal cells capturing a wide range of dendritic and perisomatic active properties. PLoS Computational Biology 7 (7), 1–18.
URL http://www.pubmedcentral.nih.gov/articlerender.fcgi?artid=3145650{&}tool=pmcentrez{&}rendertype=abstract

Helmchen, F., Sep. 2012. Calcium imaging. In: Brette, R., Destexhe, A. (Eds.), Handbook of Neural Activity Measurement. Cambridge University Press, pp. 92–135.

Holsheimer, J., 1987. Electrical conductivity of the hippocampal ca1 layers and application to current-source-density analysis. Experimental brain research 67 (2), 402–410.

Holt, G., Koch, C., 1999. Electrical interactions via the extracellular potential near cell bodies. Journal of computational neuroscience 6, 169–184.
URL http://link.springer.com/article/10.1023/A:1008832702585

Huang, Y., Parra, L. C., Haufe, S., 2016. The New York Head—A precise standardized volume conductor model for EEG source localization and tES targeting. NeuroImage 140, 150–162.
URL http://dx.doi.org/10.1016/j.neuroimage.2015.12.019

Ilmoniemi, R. J., Sarvas, J., 2019. Brain Signals - Physics and Mathematics of MEG and EEG. MIT Press, Cambridge, Massachusetts; London, England.

Jackson, J. D., 1998. Classical electrodynamics, 3rd Edition. Wiley.

Joucla, S., Yvert, B., 2012. Modeling extracellular electrical neural stimulation: from basic understanding to MEA-based applications. Journal of physiology, Paris 106 (3-4), 146–58.
URL http://www.ncbi.nlm.nih.gov/pubmed/22036892

Koch, C., 1999. Biophysics of computation: information processing in single neurons., 1st Edition. Oxford University Press: New York.

Larson, M. G., Bengzon, F., 2013. The finite element method: theory, implementation, and applications. Vol. 10. Springer Science & Business Media.

Łęski, S., Pettersen, K. H., Tunstall, B., Einevoll, G. T., Gigg, J., Wójcik, D. K., Dec. 2011. Inverse current source density method in two dimensions: inferring neural activation from multielectrode recordings. Neuroinformatics 9 (4), 401–25.
URL http://www.pubmedcentral.nih.gov/articlerender.fcgi?artid=3214268&tool=pmcentrez&rendertype=abstract

Léonetti, M., Dubois-Violette, E., Aug. 1998. Theory of Electrodynamic Instabilities in Biological Cells. Physical Review Letters 81 (9), 1977–1980.
URL http://link.aps.org/doi/10.1103/PhysRevLett.81.1977

Léonetti, M., Dubois-Violette, E., Homblé, F., Jul. 2004. Pattern formation of stationary transcellular ionic currents in Fucus. Proceedings of the National Academy of Sciences of the United States of America 101 (28), 10243–8.
URL http://www.pubmedcentral.nih.gov/articlerender.fcgi?artid=478558&tool=pmcentrez&rendertype=abstract

Łęski, S., Lindén, H., Tetzlaff, T., Pettersen, K. H., Einevoll, G. T., 2013. Frequency dependence of signal power and spatial reach of the local field potential. PLoS Comput Biol 9 (7), e1003137.

Lindén, H., Hagen, E., Łęski, S., Norheim, E. S., Pettersen, K. H., Einevoll, G. T., jan 2014. LFPy: a tool for biophysical simulation of extracellular potentials generated by detailed model neurons. Frontiers in Neuroinformatics 7 (41), 1–15.
URL http://journal.frontiersin.org/article/10.3389/fninf.2013.00041/abstract

Lindén, H., Pettersen, K. H., Einevoll, G. T., dec 2010. Intrinsic dendritic filtering gives low-pass power spectra of local field potentials. Journal of computational neuroscience 29 (3), 423–44. URL http://www.ncbi.nlm.nih.gov/pubmed/20502952

Lindén, H., Tetzlaff, T., Potjans, T. C., Pettersen, K. H., Grün, S., Diesmann, M., Einevoll, G. T., Dec. 2011. Modeling the spatial reach of the LFP. Neuron 72 (5), 859–72. URL http://www.ncbi.nlm.nih.gov/pubmed/22153380

Logg, A., Mardal, K.-A., Wells, G., 2012. Automated solution of differential equations by the finite element method: The FEniCS book. Vol. 84. Springer Science & Business Media, Berlin, Heidelberg.

Logothetis, N. K., Kayser, C., Oeltermann, A., sep 2007. In vivo measurement of cortical impedance spectrum in monkeys: implications for signal propagation. Neuron 55 (5), 809–23. URL http://www.ncbi.nlm.nih.gov/pubmed/17785187

López-Aguado, L., Ibarz, J., Herreras, O., 2001. Activity-dependent changes of tissue resistivity in the ca1 region in vivo are layer-specific: modulation of evoked potentials. Neuroscience 108 (2), 249–262.

Lopreore, C. L., Bartol, T. M., Coggan, J. S., Keller, D. X., Sosinsky, G. E., Ellisman, M. H., Sejnowski, T. J., Sep. 2008. Computational modeling of three-dimensional electrodiffusion in biological systems: application to the node of Ranvier. Biophysical journal 95 (6), 2624–35. URL http://www.pubmedcentral.nih.gov/articlerender.fcgi?artid=2527256&tool=pmcentrez&rendertype=abstract

Lu, B., Zhou, Y. C., Huber, G. a., Bond, S. D., Holst, M. J., McCammon, J. A., Oct. 2007. Electrodiffusion: a continuum modeling framework for biomolecular systems with realistic spatiotemporal resolution. The Journal of chemical physics 127 (13), 135102. URL http://www.ncbi.nlm.nih.gov/pubmed/17919055

Luo, J., Macias, S., Ness, T. V., Einevoll, G. T., Zhang, K., Moss, C. F., 2018. Neural timing of stimulus events with microsecond precision. PLoS biology 16 (10), 1–22.

Markram, H., Muller, E., Ramaswamy, S., Reimann, M. W., Abdellah, M., Sanchez, C. A., Ailamaki, A., Alonso-Nanclares, L., Antille, N., Arsever, S., et al., 2015. Reconstruction and simulation of neocortical microcircuitry. Cell 163 (2), 456–492.

Martinsen, Ø. G., Grimnes, S., 2008. Bioimpedance and Bioelectricity Basics. Academic Press; 2 edition. URL http://www.amazon.com/Bioimpedance-Bioelectricity-Basics-Second-Edition/dp/0123740045

Mazzoni, A., Lindén, H., Cuntz, H., Lansner, A., Panzeri, S., Einevoll, G. T., 2015. Computing the local field potential (lfp) from integrate-and-fire network models. PLoS Comput Biol 11 (12), e1004584.

McIntyre, C. C., Grill, W. M., Mar. 2001. Finite Element Analysis of the Current-Density and Electric Field Generated by Metal Microelectrodes. Annals of Biomedical Engineering 29 (3), 227–235.
URL http://www.springerlink.com/openurl.asp?id=doi:10.1114/1.1352640

Mechler, F., Victor, J. D., Jun. 2012. Dipole characterization of single neurons from their extracellular action potentials. Journal of computational neuroscience 32(1), 73–100.
URL http://www.ncbi.nlm.nih.gov/pubmed/21667156

Miceli, S., Ness, T. V., Einevoll, G. T., Schubert, D., 2017. Impedance spectrum in cortical tissue: Implications for propagation of lfp signals on the microscopic level. eNeuro 4 (1).
URL https://www.eneuro.org/content/4/1/ENEURO.0291-16.2016

Mitzdorf, U., 1985. Current source-density method and application in cat cerebral cortex: investigation of evoked potentials and eeg phenomena. Physiological reviews 65 (1), 37–100.

Moffitt, M. a., McIntyre, C. C., sep 2005. Model-based analysis of cortical recording with silicon microelectrodes. Clinical neurophysiology 116 (9), 2240–50.
URL http://www.ncbi.nlm.nih.gov/pubmed/16055377

Mori, Y., 2009. From three-dimensional electrophysiology to the cable model: an asymptotic study. arXiv preprint arXiv:0901.3914, 1–39.
URL http://arxiv.org/abs/0901.3914

Mori, Y., Fishman, G. I., Peskin, C. S., Apr. 2008. Ephaptic conduction in a cardiac strand model with 3D electrodiffusion. Proceedings of the National Academy of Sciences of the United States of America 105 (17), 6463–8.
URL http://www.pubmedcentral.nih.gov/articlerender.fcgi?artid=2359793&tool=pmcentrez&rendertype=abstract

Mori, Y., Liu, C., Eisenberg, R. S., 2011. A Model of Electrodiffusion and Osmotic Water Flow and its Energetic Structure. arXiv preprint arXiv:1101.5193.

Mori, Y., Peskin, C., 2009. A numerical method for cellular electrophysiology based on the electrodiffusion equations with internal boundary conditions at membranes. Communications in Applied Mathematics and Computational Science 4.1, 85–134.
URL http://msp.org/camcos/2009/4-1/p04.xhtml

Moulin, C., Glière, A., Barbier, D., Joucla, S., Yvert, B., Mailley, P., Guillemaud, R., Feb. 2008. A new 3-D finite-element model based on thin-film approximation for microelectrode array recording of extracellular action potential. IEEE transactions on bio-medical engineering 55 (2 Pt 1), 683–92.
URL http://www.ncbi.nlm.nih.gov/pubmed/18270005

Næss, S., Chintaluri, C., Ness, T. V., Dale, A. M., Einevoll, G. T., Wójcik, D. K., 2017. Corrected Four-Sphere Head Model for EEG Signals. Frontiers in Human Neuroscience 11 (October), 1–7.
URL http://journal.frontiersin.org/article/10.3389/fnhum.2017.00490/full

Nanninga, P., 2008. A computational neuron model based on Poisson-Nernst-Planck theory. ANZIAM Journal 50, 46–59.
URL http://journal.austms.org.au/ojs/index.php/anziamj/article/view/1390

Nelson, M. J., Pouget, P., may 2010. Do electrode properties create a problem in interpreting local field potential recordings? Journal of neurophysiology 103 (5), 2315–7.
URL http://www.ncbi.nlm.nih.gov/pubmed/20220081

Ness, T. V., Chintaluri, C., Potworowski, J., Łęski, S., Głąbska, H., Wójcik, D. K., Einevoll, G. T., 2015. Modelling and Analysis of Electrical Potentials Recorded in Microelectrode Arrays (MEAs). Neuroinformatics 13 (4), 403–426.
URL http://link.springer.com/10.1007/s12021-015-9265-6

Ness, T. V., Remme, M. W. H., Einevoll, G. T., 2016. Active subthreshold dendritic conductances shape the local field potential. Journal of Physiology 594 (13), 3809–3825.

Ness, T. V., Remme, M. W. H., Einevoll, G. T., 2018. h-Type Membrane Current Shapes the Local Field Potential from Populations of Pyramidal Neurons. Journal of Neuroscience 38 (26), 6011–6024.
URL http://www.jneurosci.org/lookup/doi/10.1523/JNEUROSCI.3278-17.2018

NeuroEnsamble, 2017. Elephant - electrophysiology analysis toolkit.
URL https://github.com/NeuralEnsemble/elephant

Nicholson, C., Freeman, J. A., 1975. Theory of current source-density analysis and determination of conductivity tensor for anuran cerebellum. Journal of Neurophysiology 38 (2), 356–368.

Nicholson, C., Syková, E., may 1998. Extracellular space structure revealed by diffusion analysis. Trends in neurosciences 21 (5), 207–15.
URL http://www.ncbi.nlm.nih.gov/pubmed/9610885

Niederer, S., jan 2013. Regulation of ion gradients across myocardial ischemic border zones: a biophysical modelling analysis. PloS one 8 (4), e60323.
URL http://www.pubmedcentral.nih.gov/articlerender.fcgi?artid=3618345{&}tool=pmcentrez{&}rendertype=abstract

Nunez, P. L., Srinivasan, R., 2006. Electric Fields of the Brain. Oxford University Press, New York.

Obien, M. E. J., Hierlemann, A., Frey, U., 2019. Accurate signal-source localization in brain slices by means of high-density microelectrode arrays. Scientific Reports 9 (1), 1–19.

O'Connell, R., Mori, Y., Oct 2016. Effects of glia in a triphasic continuum model of cortical spreading depression. Bulletin of Mathematical Biology 78 (10), 1943–1967.
URL https://doi.org/10.1007/s11538-016-0206-9

Pettersen, K. H., Devor, A., Ulbert, I., Dale, A. M., Einevoll, G. T., Jun. 2006. Current-source density estimation based on inversion of electrostatic forward solution: effects of finite extent of neuronal activity and conductivity discontinuities. Journal of neuroscience methods 154 (1-2), 116–33.
URL http://www.ncbi.nlm.nih.gov/pubmed/16436298

Pettersen, K. H., Einevoll, G. T., Feb. 2008. Amplitude variability and extracellular low-pass filtering of neuronal spikes. Biophysical journal 94 (3), 784–802.

URL http://www.pubmedcentral.nih.gov/articlerender.fcgi?artid=2186261&tool=pmcentrez&rendertype=abstract

Pettersen, K. H., Hagen, E., Einevoll, G. T., Jun. 2008. Estimation of population firing rates and current source densities from laminar electrode recordings. Journal of computational neuroscience 24 (3), 291–313.
URL http://www.ncbi.nlm.nih.gov/pubmed/17926125

Pettersen, K. H., Lindén, H., Dale, A. M., Einevoll, G. T., 2012. Extracellular spikes and csd. In: Brette, R., Destexhe, A. (Eds.), Handbook of Neural Activity Measurement. Cambridge University Press, pp. 92–135.

Pettersen, K. H., Lindén, H., Tetzlaff, T., Einevoll, G. T., Nov. 2014. Power laws from linear neuronal cable theory: power spectral densities of the soma potential, soma membrane current and single-neuron contribution to the EEG. PLoS computational biology 10 (11), e1003928.
URL http://www.pubmedcentral.nih.gov/articlerender.fcgi?artid=4230751&tool=pmcentrez&rendertype=abstract

Pfurtscheller, G., Cooper, R., 1975. Frequency dependence of the transmission of the EEG from cortex to scalp. Electroencephalography and Clinical Neurophysiology 38 (1), 93–96.

Pods, J., 2017. A comparison of computational models for the extracellular potential of neurons. Journal of Integrative Neuroscience 16 (1), 19–32.

Pods, J., Schönke, J., Bastian, P., Jul. 2013. Electrodiffusion models of neurons and extracellular space using the Poisson-Nernst-Planck equations–numerical simulation of the intra- and extracellular potential for an axon model. Biophysical journal 105 (1), 242–54.
URL http://www.pubmedcentral.nih.gov/articlerender.fcgi?artid=3703912&tool=pmcentrez&rendertype=abstract

Potworowski, J., Jakuczun, W., Łęski, S., Wójcik, D., feb 2012. Kernel current source density method. Neural computation 24 (2), 541–75.
URL http://www.ncbi.nlm.nih.gov/pubmed/22091662

Ranck, J. B., 1963. Specific impedance of rabbit cerebral cortex. Experimental Neurology 7 (2), 144–152.
URL http://www.sciencedirect.com/science/article/B6WFG-4GYGC4V-5/2/fb431eaa3c8ad95684a2c909cda91241

Ranta, R., Le Cam, S., Tyvaert, L., Louis-Dorr, V., 2017. Assessing human brain impedance using simultaneous surface and intracerebral recordings. Neuroscience 343, 411–422.

Reimann, M. W., Anastassiou, C. A., Perin, R., Hill, S. L., Markram, H., Koch, C., jul 2013. A biophysically detailed model of neocortical local field potentials predicts the critical role of active membrane currents. Neuron 79 (2), 375–390.
URL http://linkinghub.elsevier.com/retrieve/pii/S0896627313004431

Savtchenko, L. P., Poo, M. M., Rusakov, D. A., 2017. Electrodiffusion phenomena in neuroscience: A neglected companion.
URL http://dx.doi.org/10.1038/nrn.2017.101

Schomburg, E. W., Anastassiou, C. A., Buzsaki, G., Koch, C., aug 2012. The Spiking Component of Oscillatory Extracellular Potentials in the Rat Hippocampus. Journal of Neuroscience 32 (34), 11798–11811.
URL http://www.jneurosci.org/cgi/doi/10.1523/JNEUROSCI.0656-12.2012

Skaar, J.-E. W., Stasik, A. J., Hagen, E., Ness, T. V., Einevoll, G. T., 2020. Estimation of neural network model parameters from local field potentials (lfps). PLoS Computational Biology.

Solbrå, A., Bergersen, A. W., van den Brink, J., Malthe-Sørenssen, A., Einevoll, G. T., Halnes, G., 2018. A Kirchhoff-Nernst-Planck framework for modeling large scale extracellular electrodiffusion surrounding morphologically detailed neurons. PLoS Computational Biology 14 (10), 1–26.

Srinivasan, R., Nunez, P. L., Silberstein, R. B., 1998. Spatial filtering and neocortical dynamics: estimates of eeg coherence. IEEE transactions on Biomedical Engineering 45 (7), 814–826.

Sterratt, D., Graham, B., Gillies, A., Willshaw, D., 2011. Principles of computational modelling in neuroscience. Cambridge University Press.

Suzuki, M., Larkum, M. E., 2017. Dendritic calcium spikes are clearly detectable at the cortical surface. Nature Communications 8 (276), 1–10.
URL http://dx.doi.org/10.1038/s41467-017-00282-4

Teleńczuk, B., Dehghani, N., Le Van Quyen, M., Cash, S. S., Halgren, E., Hatsopoulos, N. G., Destexhe, A., 2017. Local field potentials primarily reflect inhibitory neuron activity in human and monkey cortex. Scientific reports 7, 40211.

Tracey, B., Williams, M., 2011. Computationally efficient bioelectric field modeling and effects of frequency-dependent tissue capacitance. Journal of Neural Engineering 8 (3).

Wagner, T., Eden, U., Rushmore, J., Russo, C. J., Dipietro, L., Fregni, F., Simon, S., Rotman, S., Pitskel, N. B., Ramos-Estebanez, C., Pascual-Leone, A., Grodzinsky, A. J., Zahn, M., Valero-Cabré, A., jan 2014. Impact of brain tissue filtering on neurostimulation fields: a modeling study. NeuroImage 85 (3), 1048–57.
URL http://www.ncbi.nlm.nih.gov/pubmed/23850466

Zangiabadi, N., Ladino, L. D., Sina, F., Orozco-Hernández, J. P., Carter, A., Téllez-Zenteno, J. F., 2019. Deep brain stimulation and drug-resistant epilepsy: a review of the literature. Frontiers in Neurology 10.